Exp Fluids (2017) 58:143
DOI 10.1007/s00348-017-2423-x

RESEARCH ARTICLE

An axisymmetric inertia-gravity wave generator

P. Maurer[1] · S. J. Ghaemsaidi[2] · S. Joubaud[1] · T. Peacock[2] · P. Odier[1]

Received: 12 April 2017 / Revised: 4 August 2017 / Accepted: 23 August 2017 / Published online: 15 September 2017

Abstract There has been a rich interplay between laboratory experimental studies of internal waves and advancing understanding of their role in the ocean and atmosphere. In this study, we present and demonstrate the concept for a new form of laboratory internal wave generator that can excite axisymmetric wave fields of arbitrary radial structure. The construction and operation of the generator are detailed, and its capabilities are demonstrated through a pair of experiments using a Bessel function and a *bourrelet* (i.e., ring-shaped) configuration. The results of the experiments are compared with the predictions of an accompanying analytical model.

1 Introduction

Laboratory experimentation has a compelling history of advancing the field of internal wave dynamics. The pioneering experiments of Görtler (1943) and Mowbray and Rarity (1967) provided the first demonstration of the peculiar internal wave dispersion relation. Early experiments studying wave generation in shear flows (Lee and Beardsley 1974) evidenced the role of nonlinearities and dispersion. These effects were studied in situ, for example by Apel et al. (1975) using satellite observations, and much more recently by Thomas et al. (2016) using pressure sensors in the Massachusetts Bay. Another example of the interplay between laboratory experiments and oceanic internal waves was the field study by Halpern (1971), regarding internal waves produced by tidal flows, which lead to experiments by Maxworthy (1979), whose results were then utilized by a number of field studies (e.g., Haury et al. 1979). The experiments by Cacchione and Wunsch (1974) studying the reflection of internal waves over a slope also provided explanations of diapycnal mixing observed in the ocean, such as in the Monterrey Canyon (Künze et al. 2012). Additional examples of synergy between experiments and field observations, focussed on wave-induced mixing, can be found in the review by Ivey et al. (2008).

The methods employed to generate internal waves in laboratory settings have evolved markedly since Görtler (1943) and Mowbray and Rarity (1967), who used an oscillating cylinder as their wave generation tool. Some prominent examples of internal wave generation mechanisms applied in the laboratory include: a single paddle extending vertically across the depth of a wave tank, which excites vertical mode structures (Cacchione and Wunsch 1974); a paddle with a localized deformation to generate wave beams (Delisi and Orlanski 1975); and oscillating topographic features cut from foam blocks to generate low mode dominated internal wave fields (Echeverri et al. 2009). Oscillations of the wave tank itself have been used to generate internal wave attractors (Maas et al. 1997), while wave paddles continue to be used, an example being the study of instabilities arising from intersecting wave beams (Teoh et al. 1997).

The aforementioned generation methods are characterized by a fixed spatial structure, which in turn limits experimental control over the spatial structure of the internal wave field. A major advance, therefore, was the advent of novel internal wave generation technology comprising a series of stacked plates driven by an eccentric cam shaft (Gostiaux et al. 2006), for which it is possible to configure the profile of the

✉ P. Odier
philippe.odier@ens-lyon.fr

[1] Univ Lyon, ENS de Lyon, Univ Claude Bernard, CNRS, Laboratoire de Physique, F-69342 Lyon, France

[2] Massachusetts Institute of Technology, 77 Massachusetts Avenue, Building 3-361b, Cambridge, MA 02139, USA

stacked plates to have the shape of a desired wave form. The capabilities of this novel wave generator technology were comprehensively investigated and demonstrated by Mercier et al. (2010), who used such a generator to produce several different canonical wave forms, including plane waves, wave beams of different cross-sectional form and vertical modes. The versatility of this wave generator has led to its use in a multitude of experiments, including studies of internal tide scattering (Peacock et al. 2009), parametric subharmonic instability (Bourget et al. 2013; Ghaemsaidi et al. 2016; Maurer et al. 2016), propagation through non-uniform stratifications (Mathur and Peacock 2009; Paoletti and Swinney 2012), and bolus generation (Moore et al. 2016).

To date, internal wave experiments have typically considered nominally two-dimensional (2D) configurations (i.e., assuming negligible variability across the experimental wave tank). Some experiments have looked into three-dimensional (3D) effects, such as the generation of a conical wave field by an oscillating sphere (Ghaemsaidi and Peacock 2013), oscillation of an axisymmetric Gaussian topographic feature (King et al. 2010), or of a horizontal torus (Ermanyuk et al. 2017) and the generation of wave beams by narrow stacked plate generators in relatively wider tanks that produce 3D mean flows (Bordes et al. 2012). In an axisymmetric configuration, Duran-Matute et al. (2013) used a torus to generate purely axisymmetric inertial waves. Messio et al. (2008) also studied the axisymmetric configuration characterizing purely inertial waves using PIV in a rotating tank. In this paper, we demonstrate the adaptation of a multi-plate wave generator to produce robust axisymmetric wave fields of arbitrary radial structure. The motivation for this arrangement is that it is quite geophysically relevant, as it pertains to the generation of near-inertial waves by storms interacting with the ocean surface (Alford 2001) and the generation of atmospheric internal waves by storm cells (Alexander et al. 1995), for which an assumption of axisymmetry is a reasonable first-order approximation that is certainly an improvement on a two-dimensional assumption. By virtue of the underlying symmetry, this advance is also naturally conducive to incorporating background rotation into the experimental investigations.

We begin, in Sect. 2, with an overview of the operational design of the wave generator and the experimental configuration, including details of the rotating table facility. Then, in Sect. 3, we present details of an axisymmetric model of internal wave generation and propagation that we have developed and use for comparison with the experimental wave fields. In Sect. 4, we present experimental results for two different configurations of the wave generator, a Bessel function and a *bourrelet* (an axisymmetric oscillating bump). Finally, we present our conclusions in Sect. 5.

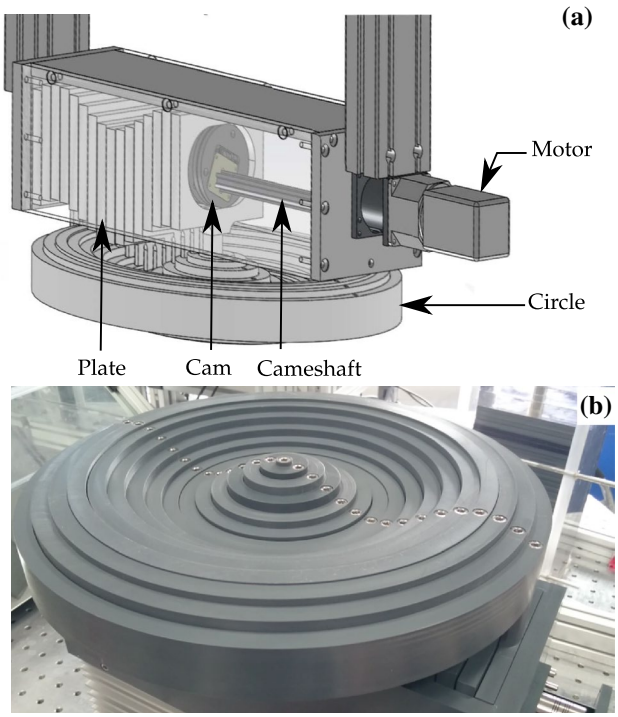

Fig. 1 **a** A schematic of the axisymmetric wave generator (with only half of the plates and cams shown, for clarity). The vertical motion of the rings is driven by the cams, which follow a sinusoidal motion at frequency ω imposed by the motor. **b** Underside view of the wave generator

2 Experimental methods

2.1 Generator design

The construction of the axisymmetric wave generator follows the underlying operational principle of Gostiaux et al. (2006) by using a series of stacked plates forced by eccentric cams to initiate internal wave disturbances. The schematic and images in Fig. 1 show that the new axisymmetric design comprises 16-, 12-mm-wide concentric, PVC rings (the central one being a 12-mm-diameter cylinder). Each ring is 38 mm high and there is a 1 mm gap between adjacent rings for flexibility; the total radius of the generator is 201 mm.

In contrast to a two-dimensional generator, for which the movement of each plate is driven by a single cam, each ring (with the exception of the central ring) is driven by two cams located equidistant from the central ring of the generator (see Fig. 1); this is necessary in order to enhance control and provide balance to the motion of the rings. To prevent jamming of the plates, aluminum guides (not drawn in Fig. 1a) are used to ensure parallel, vertical motion.

Numbering the rings 1–16 from the center to the outer ring of the generator, their prescribed vertical motion is:

$$z_n(t) = z_{0,n}\cos(\omega t + \phi_n) \quad \forall n \in [\![1, 16]\!], \tag{1}$$

where $z_{0,n}$ is the displacement amplitude of ring n (in the range 0–15 mm for our generator), ω is the rotational frequency of the camshaft, and ϕ_n is the phase of ring n (chosen by increments of $\pi/6$ for our generator). Two configurations (a Bessel function and a *bourrelet*) are used in the present paper. For each case, the value of the displacement $z_{0,n}$ and the phase ϕ_n as a function of n will be defined in Sects. 4.1 and 4.2, respectively.

This novel geometry opens up a wide range of possibilities for the excitation of different types of internal wave fields in density-stratified fluids. For example, an axisymmetric standing-wave pattern can be excited if all the phases of the plates are identical, or radially outward (inward) propagating waveforms result if the plate phases are increasing outward (inward). Imposing different amplitudes of oscillation for different rings allows for scenarios such as a strong disturbance in the center of the domain that decreases smoothly towards the outer domain.

We also note that by virtue of its geometry the device is well suited for generating purely inertial waves in rotating systems. Since the possibilities are plentiful, our goal in this paper is to provide the first demonstration of the capabilities of such a generator by visualizing some examples of inertia-gravity wave fields excited using this technology. We leave it to the interested reader to further explore the broad possibilities.

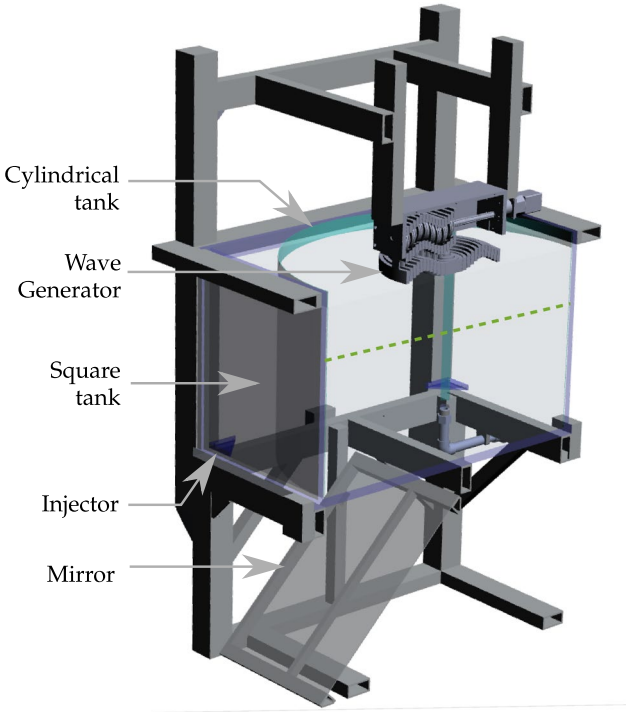

Fig. 2 Cross-sectional schematic of the experimental system comprising a transparent cylindrical tank within a square tank. The wave generator is placed above the tank, centered on the axis of rotation. The green dashed line shows the approximate position of the horizontal laser sheet in which horizontal wave velocities are measured by PIV, viewed via the tilted mirror beneath the experimental tank

2.2 Experimental arrangement

Our experiments were conducted in a cylindrical Plexiglas tank that was housed within a transparent Plexiglas tank of square cross section (see Fig. 2). Salt-stratified water resided both inside and outside of the cylinder, preventing significant optical deformations for the visualization system. In setting the scale of the system, an important consideration was that viscous damping for inertia-gravity waves scales as the cube of the wave-vector amplitude. To try and lessen the impact of viscous damping, our square external tank had sides of length 1 m, enabling the inner cylindrical tank to be 1 m in diameter; both tanks were 0.6 m in height. A series of horizontal holes were drilled around the lower section of the cylindrical tank to allow fluid to flow freely between the two chambers during filling from below.

The tank structure was mounted on a turntable (denoted as PERPET, designed and constructed by GP Concept) that was 1.92 m in diameter. The rotational velocity could be set in the range $0 < \Omega < 60$ rpm with an accuracy of 0.1%, which corresponds to a Coriolis parameter $f = 2\Omega$ in the range $0 < f < 12.5\,\mathrm{rad\,s^{-1}}$. The axis of rotation was vertically aligned with gravity with a tolerance of 2 mm $\mathrm{m^{-1}}$. A salt stratification was established using the standard double bucket method (Fortuin 1960; Oster and Yamamoto 1963) with buoyancy frequency $N \approx 1\,\mathrm{rad\cdot\,s^{-1}}$.

The tank was filled while at rest and then spun up very slowly, at an angular acceleration rate less that 10^{-3} rad $\mathrm{s^{-2}}$, in order to prevent mixing from degrading the stratification. Since a vertical density gradient suppresses vertical fluid motion, the typical timescale to achieve solid body rotation is longer for a stratified fluid than for a homogeneous fluid, for which three-dimensional flows such as Ekman pumping distribute momentum from the rotating base of the tank into the body of the fluid that is initially at rest. In the most extreme case, a body of stratified fluid will be set in rotation by viscosity alone. In this case, assuming that the flow is purely azimuthal and that there is no variation of the velocity in z (case of an infinitely high cylinder), the azimuthal velocity v_θ is the solution to:

$$\frac{\partial v_\theta}{\partial t} = \nu \Delta v_\theta, \tag{2}$$

where ν is the kinematic viscosity. Figure 3a presents histories of the horizontal velocity at a point in the bulk ($r = 29$ cm) undergoing external rotation (in the case of the stratified fluid, the horizontal velocity $v_h = \sqrt{v_\theta^2 + v_r^2}$

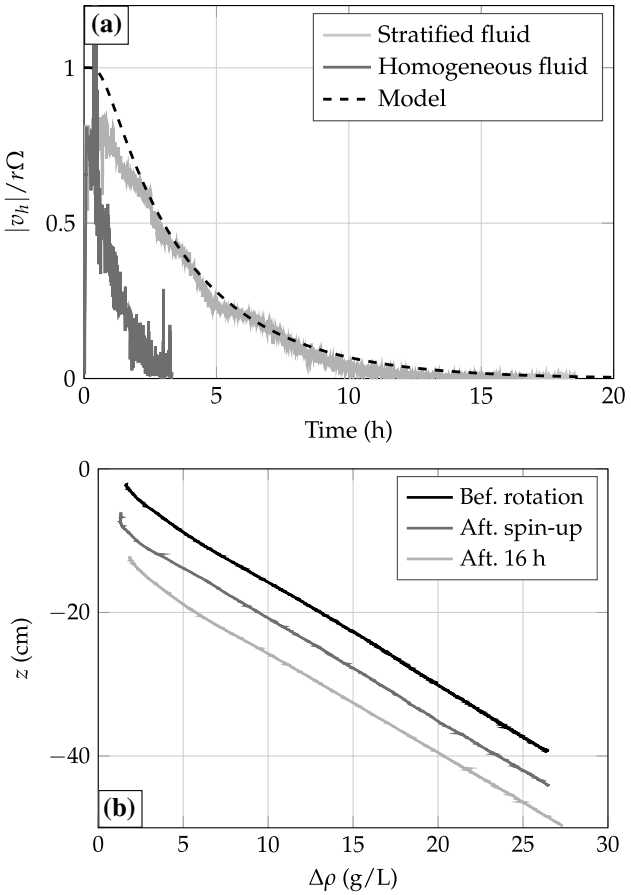

Fig. 3 **a** Magnitude of the horizontal velocity of the fluid $|v_h|$ (in the stratified case, $v_h \simeq v_\theta$) for the flow at radius $r = 29$ cm while the turntable is spun up to a rotation rate $\Omega = 0.125$ rad s^{-1}, for a homogeneous (black line) and a stratified (gray line) fluid. In the case of the stratified fluid, the measurements are in agreement with the solution to Eq. (2) (dashed line), which only considers the viscous diffusion of momentum from the sidewalls. **b** A sample stratification measured before rotation, after the turntable has completed its acceleration to an angular velocity of $\Omega = 0.125$ rad s^{-1} in 240 s, and after 16 h of rotation at constant angular velocity $\Omega = 0.125$ rad s^{-1}; a vertical offset of 5 cm has been introduced between the three profiles to aid visual comparison

reduces to v_θ, since radial motion is negligible). Once the momentum induced by the rotation of the tank walls is fully diffused, we expect the velocity to vanish in the rotating frame. As expected, the momentum diffusion time was notably shorter for a homogeneous fluid (~2.5 h) than for a stratified fluid (~15 h). Equation (2) was solved using a classical solver, assuming a no-slip boundary condition at the edge ($r = 0.5$ m) and vanishing velocity at the center. The solution at $r = 29$ cm—the radius where the velocity was measured—is included in Fig. 3a and is in good agreement with the measurements for a stratified fluid; viscosity is therefore the dominant force that drives the stratified fluid into rotation. Furthermore, the stratified experiments confirmed that radial velocity is negligible in comparison to the azimuthal velocity, which confirms the applicability of Eq. (2). To demonstrate the minimal impact of spin-up on the initial stratification, Fig. 3b presents an example of a density profile before rotation, after spin-up of the table, and after 16 h of constant rotation at $\Omega = 0.125$ rad s^{-1}. It is clear that even on a timescale much larger than the typical experimental time (~20 min), the variation of N is negligible. We also checked that the bending of the isopycnal, due to rotation, was negligible; at maximum speed (~0.8 rad s^{-1}), the variation in depth over the 50 cm tank radius is smaller than 1 cm. The profile is measured at the edge of the tank.

Particle image velocimetry (PIV) was used to measure the experimental velocity field. A laser sheet was created by passing a 2-W Ti:sapphire laser (Laser Quantum) with a 532-nm wavelength through a cylindrical lens. The laser sheet could be oriented both vertically and horizontally, with the former passing through the central axis of the rotation table (with visualization taking place through a normal facing side of the tank), and the latter requiring visualization through the tank base via a 45° inclined mirror (see Fig. 2). When the laser sheet was positioned vertically, the fluid was seeded with a concentration of 3.3 mg L^{-1} of hollow glass spheres (manufactured by Sphericel, with 1.1 kg L^{-1} density, and 10 µm diameter); when the laser sheet was oriented horizontally, the fluid was seeded with a concentration of 0.8 mg L^{-1} of silver-coated hollow glass spheres (manufactured by Dantec Dynamics, with 1.4 kg L^{-1} density, and 10 µm diameter). Experiments involving a horizontal laser sheet require seed particles with more reflectivity given that the scattered light has to travel through the 3-cm-thick tank bottom, which oftentimes has a layer of sedimented particles above it. The CIVx algorithm (Fincham and Delerce 2000) combined with UVMAT software[1] was used to compute the cross-correlation between two successive images, giving, in the case of the vertical sheet, the instantaneous vertical and radial velocities, and in the case of the horizontal sheet, the instantaneous azimuthal and radial velocities. The maximum opening angle of the camera relative to the laser sheet was 20°, which largely suppressed parallax. Moreover, a sufficiently high image acquisition rate was chosen (~4 Hz) in order to minimize the out-of-plane particle displacement between successive images. Images were recorded using a Allied Vision Pike F-505 camera (maximal resolution of 2452 (H) × 2054 (V)) and 12.5-mm focal lens located at 130 cm from the middle of the tank, leading to a 0.36 mm/pixel resolution and a maximum field of view of 88 × 74 cm^2.

Note also that in this paper, we focus on the wave field observed around 20 oscillation periods after the wave generator was started. We checked that at that time, the transient

[1] J. Sommeria, LEGI / CNRS-UJF-INPG, http://servforge.legi.grenoble-inp.fr/projects/soft-uvmat.

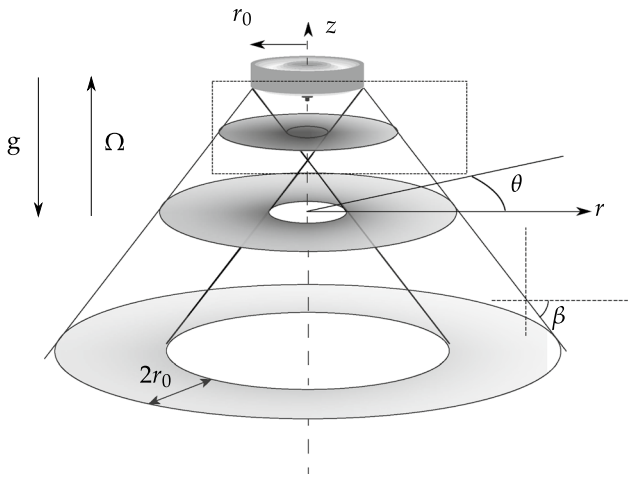

Fig. 4 A schematic illustrating the structure of the inertia-gravity wave field radiated at a fixed frequency ω in a constant N stratification, subject to the dispersion relation (3). For an initial forcing of finite radius r_0, the wave field is expected to primarily reside within a ring of width $2r_0$, with the radius of the ring increasing linearly with depth, thereby forming a conical shape. The dashed square illustrates the typical location of the field of view (aspect ratio not conserved) in our experiments

stage is almost finished and a saturation in amplitude in the zone of measurement is observed, while no reflected waves coming from the side and/or the bottom appear yet on the field of view and disturb the wave field (they appear after about 50 oscillation periods).

3 Analytical model

To investigate the quality of the wave fields produced by the wave generator, we consider an axisymmetric model of inertia-gravity wave generation and propagation in the presence of a background stratification, $N(z)$, and background rotation, f. In contrast to two-dimensional models, for which the horizontal basis functions are naturally Fourier modes (Mathur and Peacock 2009), an axisymmetric system is characterized by Bessel functions. Figure 4 presents a schematic of the basic geometry of a wave field that originates from an axisymmetrically configured generator driven at a fixed frequency, ω, in a linear stratification (i.e., constant N). In such a configuration the inertia-gravity waves are emitted at a fixed angle β (defined in Fig. 4) relative to the horizontal according to the inertia-gravity wave dispersion relation:

$$\omega^2 = N^2 \sin^2\beta + f^2 \cos^2\beta. \tag{3}$$

Due to the finite extension of the generator, the energy of the wavefield focuses along a conical shape.

3.1 Governing equations

Following earlier derivations such as in Flynn et al. (2003) and Davis and Smith (2010), we begin by directly adopting a cylindrical coordinate system to model our experiment. Small-amplitude, axisymmetric inertia-gravity waves in a viscous, Boussinesq, density-stratified fluid with constant background rotation satisfy the following system of governing equations:

$$\partial_t v_r = f v_\theta - \frac{1}{\rho_0}\partial_r p + \nu \Delta_h v_r, \tag{4}$$

$$\partial_t v_\theta = -f v_r + \nu \Delta_h v_\theta, \tag{5}$$

$$\partial_t v_z = -\frac{\rho'}{\rho_0} g - \frac{1}{\rho_0}\partial_z p + \nu \Delta_z v_z, \tag{6}$$

$$\partial_t \rho' = \frac{v_z N(z)^2 \rho_0}{g}, \tag{7}$$

$$0 = \frac{1}{r}\partial_r (r v_r) + \partial_z v_z, \tag{8}$$

where $\mathbf{v}(r,z,t) = (v_r, v_\theta, v_z)$ is the velocity field with radial (r), azimuthal (θ) and vertical (z) components, ρ' is the perturbation to the background density $\bar{\rho}(z)$, p is the pressure perturbation, $N(z)=\sqrt{(-g/\rho_0)\partial\bar{\rho}/\partial z}$ is the background buoyancy frequency, ρ_0 is a reference background density and $f = 2\Omega$ is the Coriolis frequency for a given background rotation frequency Ω. Δ_h represents the vector laplacian projected in the horizontal (radial or orthoradial) directions, while Δ_z is the vector laplacian in the axial direction.[2] We assume the absence of any azimuthal variation, i.e., $\partial_\theta \approx 0$; this assumption does not prohibit the existence of an azimuthal velocity component v_θ, as will be shown later.

Using the combined equations ∂_{tz} (4), (5), ∂_{tr} (6) and (7), and eliminating common terms between these four equations, we obtain[3]

$$\begin{aligned}\partial_{ttz} v_r - \partial_{ttr} v_z = {} & N(z)^2 \partial_r v_z - f^2 \partial_z v_r \\ & + \nu \Delta_h (\partial_{tz} v_r - \partial_{tr} v_z + f \partial_z v_\theta).\end{aligned} \tag{9}$$

Furthermore, introducing an axisymmetric stream function Ψ that satisfies (8),

[2] The mathematical expressions for the vector laplacian of X in the cylindrical coordinates are $\Delta_h X = \frac{\partial^2 X}{\partial z^2} + \frac{\partial^2 X}{\partial r^2} + \frac{1}{r}\frac{\partial X}{\partial r} - \frac{X}{r^2} = \frac{\partial^2 X}{\partial z^2} + \partial_r\left(\frac{1}{r}\partial_r (rX)\right)$ and $\Delta_z X = \frac{\partial^2 X}{\partial z^2} + \frac{\partial^2 X}{\partial r^2} + \frac{1}{r}\frac{\partial X}{\partial r}$.

[3] Note that, mathematically $\partial_r \Delta_z = \Delta_h \partial_r$.

$$v_r = -\frac{1}{r}\partial_z(r\Psi), \tag{10}$$

$$v_z = \frac{1}{r}\partial_r(r\Psi), \tag{11}$$

Eq. (9) becomes

$$\begin{aligned} &-\partial_{tt}\left[\partial_{zz}\Psi + \partial_r\left(\frac{1}{r}\partial_r(r\Psi)\right)\right] = N(z)^2\partial_r\left(\frac{1}{r}\partial_r(r\Psi)\right) \\ &+f^2\partial_{zz}\Psi + \nu\Delta_h\left[-\partial_{tzz}\Psi - \partial_{tr}\left(\frac{1}{r}\partial_r(r\Psi)\right) + f\partial_z v_\theta\right]. \end{aligned} \tag{12}$$

Using the expression of the vector laplacian projected along the horizontal direction, one can rewrite Eq. (12)

$$\begin{aligned} -\partial_{tt}\Delta_h\Psi = \; & N(z)^2\Delta_h\Psi + (f^2 - N(z)^2)\partial_{zz}\Psi \\ & +\nu\Delta_h\left[-\partial_{tzz}\Psi - \partial_{tr}\left(\frac{1}{r}\partial_r(r\Psi)\right) + f\partial_z v_\theta\right]. \end{aligned} \tag{13}$$

The linearity of the governing equations allows for particular modes to be independently studied. First, we do a Fourier transform in time, and consider only harmonic solutions. Using the axisymmetry of the experiment, the wave field can be expressed, without loss of generality, as the weighted sum of an infinite number of Bessel functions of the first kind. For the specific problem under consideration, the first-order Bessel function, J_1, is an eigenmode of the horizontal projection of the laplacian operator, Δ_h.

We therefore take Ψ to be a harmonic solution incorporating a radial first-order Bessel function, J_1:

$$\Psi(z, r, t) = \psi(z)J_1(kr)\exp(-\mathrm{i}\omega t), \tag{14}$$

where $\psi(z)$ is the vertical structure of the wave field.[4]

Combining Eqs. (10) and (11) with well-known relations between Bessel functions and their derivatives, the velocities are expressed as:

$$v_r = -\psi'(z)J_1(kr)\exp(-\mathrm{i}\omega t), \tag{15}$$

$$v_z = k\psi(z)J_0(kr)\exp(-\mathrm{i}\omega t). \tag{16}$$

Note that this choice is consistent with mass conservation, since we must have $v_r = 0$ at $r = 0$.

3.2 Inviscid solution

In the inviscid case, v_θ is given by

$$v_\theta = \frac{-\mathrm{i}f}{\omega}\psi'(z)J_1(kr)\exp(-\mathrm{i}\omega t), \tag{17}$$

and Eq. (12) becomes

$$\psi''(z)(-\omega^2 + f^2) + \psi(z)k^2(\omega^2 - N(z)^2) = 0. \tag{18}$$

For a constant stratification (i.e., $N(z) = N_0$), the solution of this equation is proportional to $\exp(\mathrm{i}mz)$, with the vertical wavenumber m satisfying the dispersion relation:

$$m(k, \omega) = \pm k\left(\frac{N_0^2 - \omega^2}{\omega^2 - f^2}\right)^{1/2}. \tag{19}$$

We note that Eq. (19) corresponds to the dispersion relation in Eq. (3), where $\beta = \arctan(k/m)$. Thus, the general solution for Eq. (12), in the inviscid limit, is of the form:

$$\Psi = \Psi_0\exp(\mathrm{i}mz)J_1(kr)\exp(-\mathrm{i}\omega t), \tag{20}$$

where Ψ_0 is a constant wave amplitude.

3.3 Weakly viscous solution

In our experiments, viscous effects are small but not entirely negligible. The following derivation takes viscosity into account at first order in $\epsilon = \nu k^2/\omega \ll 1$. Since v_θ, described at order zero by Eq. (17), appears only at first order in Eq. (12), incorporating a viscous correction in v_θ would yield an unnecessary second-order correction. It is thus sufficient to keep v_θ at zero order (without a viscous correction) via Eq. (17).

Inserting Eq. (14) into Eq. (12) and using Eq. (17) for v_θ yields the fourth differential equation

$$\begin{aligned} &\psi''''(z)\mathrm{i}\nu\left[\omega - \frac{f^2}{\omega}\right] + \psi(z)k^2[\omega^2 - N(z)^2 + \mathrm{i}\nu\omega k^2] \\ &+\psi''(z)\left[-\omega^2 + f^2 - \mathrm{i}\nu k^2\left(2\omega - \frac{f^2}{\omega}\right)\right] = 0. \end{aligned} \tag{21}$$

Equation (18) is the limiting case ($\nu = 0$) of Eq. (21).

For a constant stratification ($N(z) = N_0$) and in the presence of weak viscosity, the modal solutions have the approximate form

$$\Psi = \Psi_0\exp(\mathrm{i}\mathcal{M}z)J_1(kr)\exp(-\mathrm{i}\omega t), \tag{22}$$

where

$$\mathcal{M}(k, \omega) = m(k, \omega) + \epsilon m^\nu(k, \omega), \tag{23}$$

m is the inviscid vertical wavenumber given by (19), and m^ν is a weakly viscous correction. The explicit expression for this term is

$$m^\nu(k, \omega) = \pm\mathrm{i}\frac{k}{2}\frac{N_0^2(N_0^2 - f^2)}{(\omega^2 - f^2)(N_0^2 - \omega^2)}\sqrt{\frac{N_0^2 - \omega^2}{\omega^2 - f^2}}. \tag{24}$$

Such a correction of the dispersion relation due to viscosity is already known for plane waves (Lighthill 1978). From

[4] The choice of the first-order Bessel function, combined with expression (14) leads to $\Delta_h\Psi = -k^2\Psi + \partial_{zz}\Psi$.

expression (24), we can compute that for all the experiments to be compared with the model, the typical viscous dissipation length is generally of the order of a few meters, therefore we can conclude that viscous effects do not play a major role in these experiments. For this reason, we use the inviscid model in what follows.

3.4 General solution

The modal solutions presented in Sect. 3.2 enable a standard procedure to predict the entire wave field in an experimental domain, using its radial structure at a given depth as a boundary condition. From a time series of the vertical velocity at a given depth (which we take to be $z = 0$), one computes the Fourier transform in time and the zeroth-order Hankel transform in the radial direction; this transform gives a measurement of the amplitude of each temporal and spatial mode, which we will denote $\tilde{\Psi}_{k,\omega}(z = 0)$. Note that we use the time series of the vertical velocity component, rather than the radial velocity component, in order to obtain a direct measurement of ψ (see Eq. (16)). One should note that such decomposition in axisymmetric modes is mathematically identical to the decomposition of two-dimensional, vertically confined internal waves. In the axisymmetric scenario, the confinement is imposed by $v_r = 0$ at $r = 0$ and $r = \infty$. The radial velocity of a general axisymmetric wave field can therefore be decomposed into an infinite sum of first-order Bessel functions.

In the case of a constant stratification, which is the scenario we consider in this paper, the solution is given by the vertical propagation of each mode $\tilde{\Psi}_{k,\omega}$ according to Eq. (18), yielding

$$\Psi(z, r, t) = \int k\mathrm{d}k\mathrm{d}\omega \tilde{\Psi}_{k,\omega}(z = 0) \exp[\mathrm{i}m(k, \omega)z] J_1(kr) \exp(-\mathrm{i}\omega t). \tag{25}$$

More generally, in an arbitrary stratification, each mode $\tilde{\Psi}_{k,\omega}(z)$ propagates according to Eq. (18) and the formal solution is:

$$\Psi(z, r, t) = \int k\mathrm{d}k\mathrm{d}\omega \tilde{\Psi}_{k,\omega}(z) J_1(kr) \exp(-\mathrm{i}\omega t). \tag{26}$$

4 Results

We investigated two different types of forcing: one with a radial profile of a Bessel function, and a second type of forcing mimicking an axisymmetric bump, which we refer to as a *bourrelet* configuration. As we have shown in the previous section, the first configuration, that of the Bessel function, is a natural mode to describe axisymmetric wave fields. The second configuration, i.e., the bourrelet, enables geometric focusing which has the propensity to yield intriguing nonlinear effects.

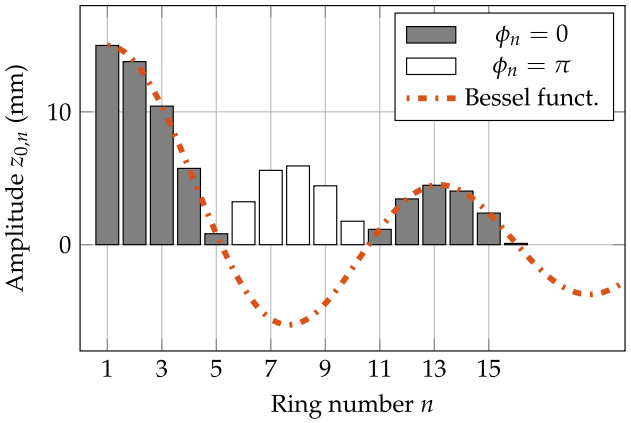

Fig. 5 Amplitudes and phases of the cams for the Bessel function configuration. The dashed orange line represents the Bessel function used to calculate the plate amplitude with a wavenumber $k_{\mathrm{gen}} = 42\ \mathrm{m}^{-1}$

4.1 Bessel function forcing

This configuration aims at reproducing a zeroth-order Bessel function for the vertical velocity, although the finite extent of the generator naturally results in a mildly truncated Bessel function. To keep the spatial scale large enough that viscous effects are weak, we chose to reproduce the Bessel function over one and a half "wavelengths"; Fig. 5 shows the amplitude and phase designated to each ring. The profile was scaled with an amplitude of 15 mm for the center ring.

Cross sections of the vertical and radial velocity components of the wave field, obtained in the vertical plane containing the central axis of the generator ($r = 0$), are presented in Fig. 6. The symmetry and antisymmetry of the respective vertical and radial velocity fields, with respect to the $r = 0$ centerline, as reflected in Eqs. (15) and (16), can be clearly observed. Along the $r = 0$ centerline, the vertical velocity is a decaying sinusoid, as expected for an outward propagating Bessel function. Outside of the central region of the domain, the wave field is oriented at an angle β with respect to the horizontal. This clearly defined angle is a sign of temporal monochromaticity, which is further confirmed by the frequency spectrum of the wave field (presented in Fig. 7a). One must note that, as shown in Fig. 4, the experimental field of view captures only a narrow region near the top of the cone. For this reason, the decay in z on the central axis, due the spreading of the wave along the cone, is barely observable. It can be, however, seen at depths below $z \simeq -50$ cm.

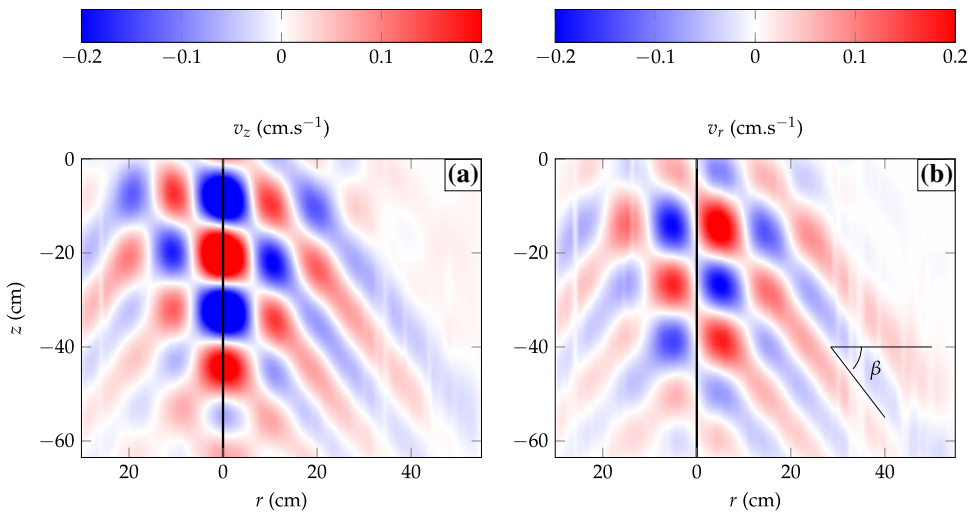

Fig. 6 PIV images of the **a** vertical and **b** radial velocity fields for a wave field radiating from a generator (located at $z = 0$ and centered at $r = 0$) configured with the Bessel function form presented in Fig. 5: $k_{gen} = 42$ m^{-1}, $a = 15$ mm for the center ring, $\omega/N = 0.79$ and $f/N = 0.2$

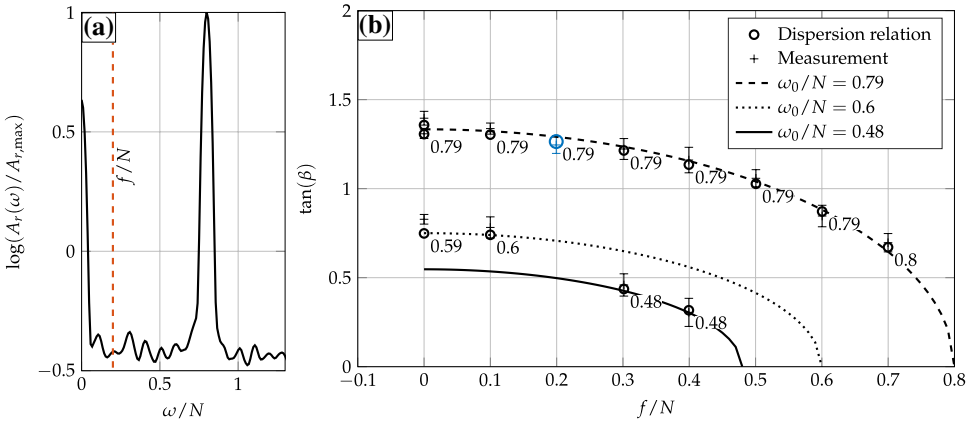

Fig. 7 **a** Temporal Fourier transform of the radial velocity, measured in a vertical plane (for the same wave shown in Fig. 6) over 500 images, corresponding to a 250-s time window. The dashed line represents $\omega/N = f/N = 0.2$. **b** A comparison of the direct measurement of $\tan\beta$ from spatial images like those shown in Fig. 6, and the expected values of $\tan\beta$ using the dispersion relation (19); the value of ω/N used for each experiment is indicated next to each data point. The solid, dotted and dashed lines plot the dispersion relation (3) for $\omega_0/N = 0.48$, 0.6 and 0.79, respectively. The larger blue circle in **b** shows the experiment of Figs. 6 and 10

From snapshots of the wave field, we can confirm the expected dispersion relation (3) for the generated waves. With N and f known, the angle β can be extracted directly from the velocity snapshots by plotting the iso-phase lines, while ω can be confirmed by obtaining a temporal Fourier spectrum from the time histories, such as that presented in Fig. 7a. As shown in Fig. 7b, the measured $\tan\beta$ quantity, determined using spatial images like those shown in Fig. 6, and the expected $\tan\beta$ quantity, determined via the dispersion relation given by Eq. (19), are in excellent agreement across a wide number of experiments with varying values of ω/N and f/N. As such, we conclude that the wave field produced by the generator is indeed propagating according to the linear inertia-gravity waves dispersion relation. Such result was expected since the dispersion relation in rotating and stratified fluid was previously checked by Peacock and Weidman (2005) when studying waves generated by a vertically oscillating sphere.

Next we consider the horizontal structure of the wave field, with the goal of checking the axisymmetry, as well as the existence of an azimuthal velocity component; the experimental setup allows for such observations through the use of a 45° mirror. Figure 8 presents velocity field measurements obtained in a horizontal plane 10 cm below the generator. As expected, the velocity field is indeed quite axisymmetric, although with some minor imperfections. In the non-rotating case, the azimuthal velocity is negligible, whereas in the rotating case it is well established, as predicted by Eq. (17). Comparing Fig. 8a, c, one can also observe that the radial decay appears stronger in the non-rotating case; this is due to the more shallow propagation angle of waves in the rotating case, which

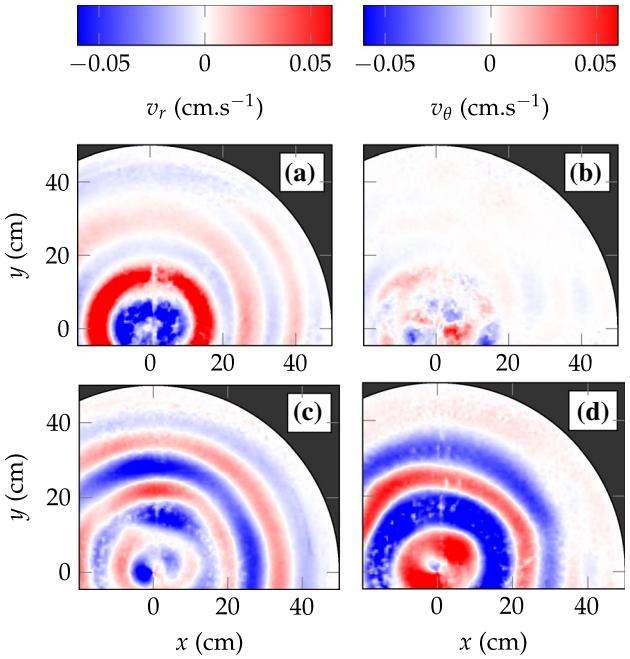

Fig. 8 Wave field velocities in the horizontal plane at $z = 10$ cm; the wave generator, forcing at $\omega/N = 0.5$, is centered at $(x, y) = (0, 0)$ cm. The left and right columns depict the radial and azimuthal velocity fields, respectively; panels **a**, **b** have no rotation, whereas **c**, **d** correspond to $f/N = 0.3$. The area shaded black is external to the experimental cylinder

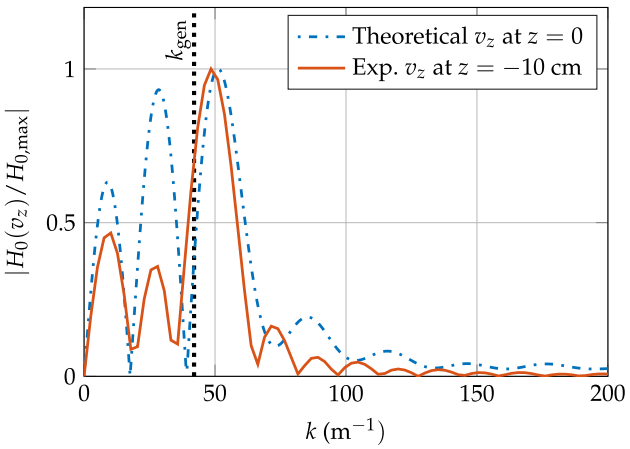

Fig. 9 Zeroth-order Hankel transform of the truncated Bessel function used for the wave generator profile (dashed-dotted blue line), and the radial profile of the vertical velocity at $z = -10$ cm (solid red line). The black dotted line shows the value k_{gen} of the Bessel function used to set the wave generator profile

results in a larger overlap between the intersecting image plane and the wave cone.

In further assessing the Bessel-function nature of the radiated wave field, we note that the forcing was actually not a true Bessel function, but rather a truncated Bessel function due to the absence of experimental forcing for $r > 20$ cm. To investigate the effect of this truncation, we compared the zeroth-order Hankel transform of the wave generator profile and the radial profile of a typical experiment, the result of which is presented in Fig. 9. The zeroth-order Hankel transform of a pure Bessel function is simply an isolated peak at k_{gen}, whereas truncation of the Bessel function beyond the first couple of wavelengths introduces several secondary peaks while maintaining a dominant peak around k_{gen} in the corresponding zeroth-order Hankel transform. The zeroth-order Hankel transform of the experimental radial profile of v_z at $z = -10$ cm displays the same characteristics associated to the truncated Bessel function, with particularly nice agreement at the primary peak closest to k_{gen}. The two peaks at $k < k_{gen}$ are also present, although with smaller amplitudes compared to the theoretical peaks. Interestingly, the transform of the experimental profile does not show any peak around $k = 500$ m^{-1} (not shown in the figure), which corresponds to the thickness of the individual rings that make up the wave generator. This confirms that the discretization of the forcing profile via plates of finite thickness has negligible impact on the generated wave field, in line with the findings of Mercier et al. (2010). This is also expected, due to the fact that the viscous attenuation of high wavenumber components of the waves is much stronger.

We now use the procedure described in Sect. 3, in particular Eq. (25), to make direct comparisons between our axisymmetric model and experiments. To begin, we recorded a time series of the vertical velocity at a depth 10 cm below the generator. This particular depth was chosen because it was not too far from the generator while close enough to provide reliable measurements. Closer to the generator the wave cone is not as clean because of the mixing and mean current induced by the motion of the generator. For modeling purposes, the experimental field at this depth was used as boundary condition to solve Eq. (25), giving access the theoretical wave field at all depths below this level. Figure 10 presents a comparison of the experimental and theoretical velocity fields in a vertical plane. Overall, the analytical solutions compare very favorably to the experimental observations, except for small-scale features which we attribute to measurement noise in the experimental data. More detailed comparisons involving velocity field profiles are presented in Fig. 11, which plots radial profiles of the radial and vertical velocity envelopes obtained at depths $z = -20, -30, -40$ and -50 cm. There is, as expected, a very close match at $z = -20$ cm, which is the profile positioned closest to the wave generator. We observe consistently good agreement between theory and experiment over the four depths studied, with one notable difference being the prediction of the vertical velocity near the centerline at $z = -30$ cm. There are several possible reasons for this observed difference, including a slight non-axisymmetric nature of the experimental

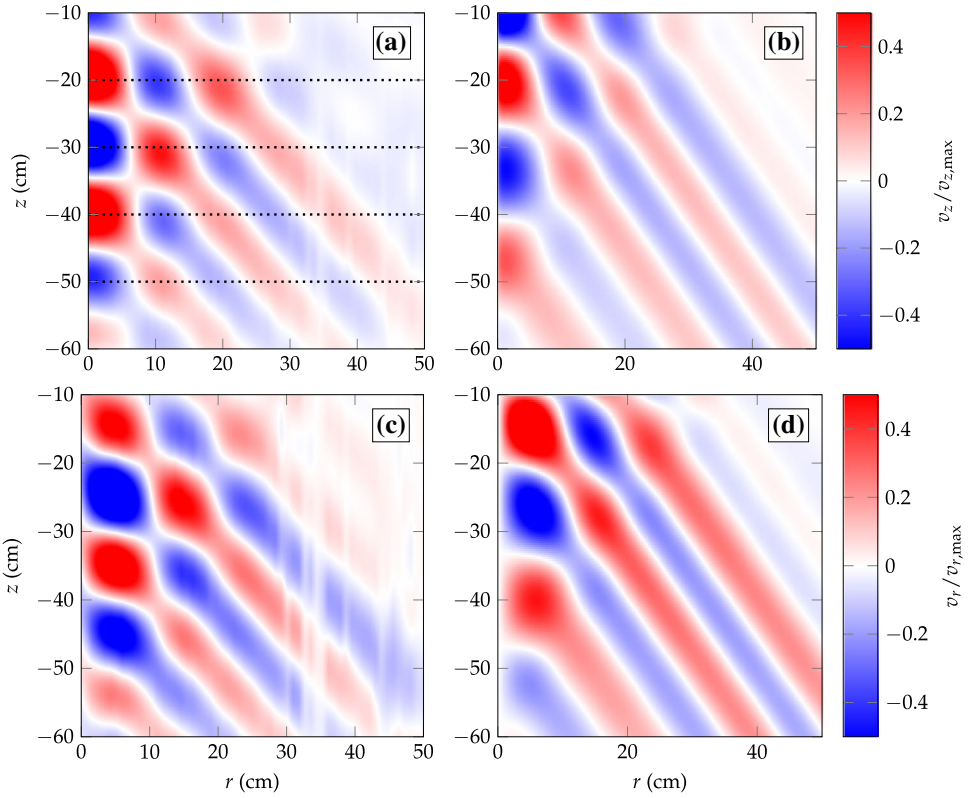

Fig. 10 Experimental measurements of the vertical (**a**) and radial (**c**) velocities in a vertical plane passing through the central axis of the generator. **b**, **d** Corresponding theoretical predictions using Eq. (25). The generator is set as a Bessel function, with $\omega/N = 0.79$ and $f/N = 0.2$. Dashed lines represent the vertical levels used to plot the amplitude envelopes presented in Fig. 11. The generator is located at $z = 0$

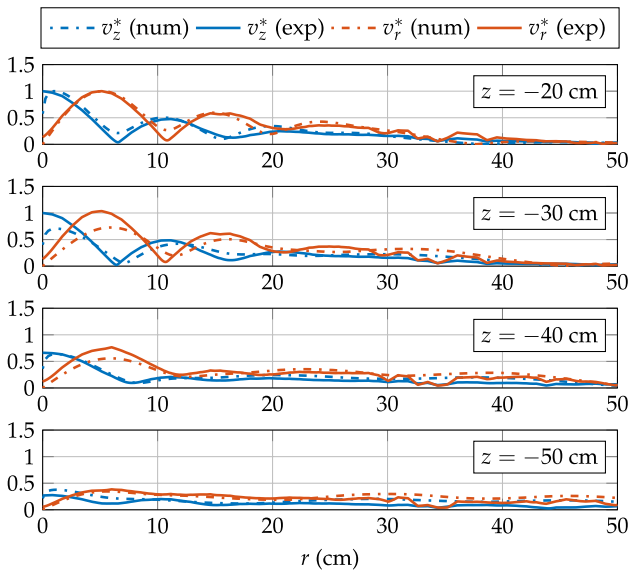

Fig. 11 Comparisons of experimental and theoretical velocity amplitude envelopes (defined as v^* to differentiate them from the velocity itself) of vertical and radial velocities, at $z = -20, -30, -40$, and -50 cm (for the experiment shown in Fig. 10). Data have been normalized by the peak amplitude at $z = -10$ cm. Solid and dashed lines represent theoretical and experimental velocities, respectively

wave field due to an offset of the generator or a weak background flow, whether naturally present in the rotating tank or induced by the forcing of the generator.

Lastly, we investigate the efficiency of the wave generator in transmitting waves to the fluid bulk. This efficiency can be defined as the ratio between the induced wave vertical velocity $v_z(z_0)$, measured at a given depth z_0, and the imposed generator vertical velocity amplitude $a\omega$, where a is the generator Bessel amplitude a. In order to neglect viscous damping, measurements were obtained at depth $z_0 = -5$ cm, the closest position where we could obtain reliable PIV data. Based on the computation of the viscous correction m^ν expressed in Eq. (24), most data points in this measurement are unaffected by viscous effects, except the points at lowest frequency ω/N (below 0.4), which can explain the relative decrease of efficiency (compared to the theoretical curves) for these data points. Our results are presented in Fig. 12 as a function of forcing frequency for three different background rotation rates. At constant f, the efficiency increases with ω, related to the fact that the waves are more vertical and therefore more aligned with the motion of the generator rings. At constant ω, the efficiency decreases with background rotation. An increase in the background rotation

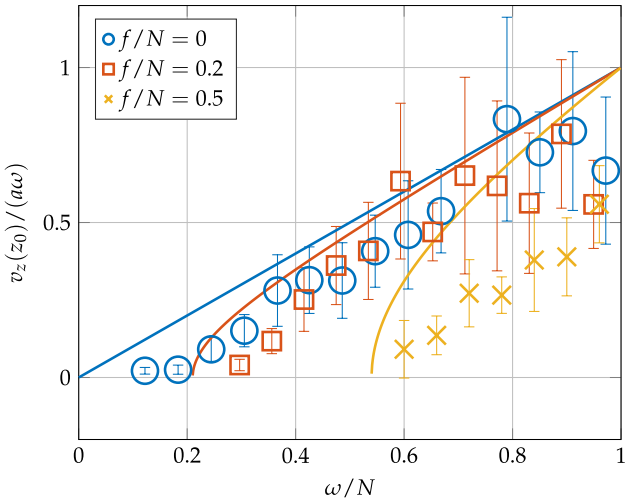

Fig. 12 Measurements of wave generator efficiency $v_z(z_0)/a\omega$ as a function of forcing frequency for three different background rotation rates. The solid lines represent $V_{z,max}/(a\omega)$

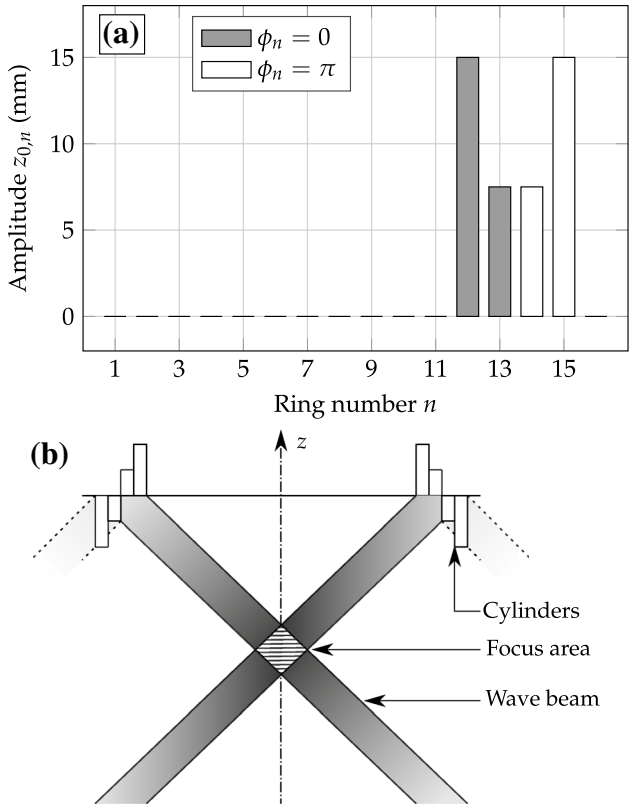

Fig. 13 **a** Amplitudes and phases of the cams for the wave generator set as a *bourrelet*. **b** Schematic of the wave emitted from a *bourrelet* and focus area where the amplitude of the wavefield is increased by geometric focusing

rate yields a stronger azimuthal velocity field (as observed in Fig. 8d), and the accommodation of v_θ subsequently weakens the other two velocity components, v_r and v_z, thereby diminishing the efficiency of the wave generator. We note that the azimuthal velocity field is not imposed by the generator, but rather is induced by the external rotation. For an imposed vertical velocity $a\omega$, the maximum vertical velocity component as a function of f and ω is

$$V_{z,max} = a\omega\sqrt{\frac{\omega^2 - f^2}{N^2 - f^2}}. \tag{27}$$

From Fig. 12, we see that the measured efficiencies are consistently less than the maximum attainable efficiencies given by Eq. (27). Moreover, the difference between the two increases with growing background rotation, which is to be expected given how the experimental velocity field must adjust to accommodate an induced azimuthal component.

4.2 *Le bourrelet* forcing

For our second experimental study, we considered the configuration of the generator shown in Fig. 13a, in which the excitation is localized over four of the outer rings. This arrangement was chosen in order to produce a localized wave cone focused onto the central axis. Figure 13b shows that a generated wave cone will be subject to a large increase in intensity thanks to geometric focusing. It thus provides a novel way to create a controlled, intense, localized wave field that is the axisymmetric analog of the wave fields that have been studied by looking at colliding internal wave beams (Teoh et al. 1997; Smith and Crockett 2014). While similar experiments have been performed using a vertically oscillating torus (Duran-Matute et al. 2013), our setup allows for more controlled wave generation with respect to shape and amplitude.

Figure 14a, c presents the vertical and radial velocities of the wave cones emitted from the *bourrelet* arrangement; corresponding analytical solutions are presented in Fig. 14b, d, respectively, following the same procedure described in Sect. 4. The spatial frequencies of the *bourrelet* is shown in Fig. 15. We observe good agreement between the spatial frequencies of the *bourrelet* forcing and the vertical velocity field transmitted at $z = -10$ cm. As in the Bessel mode case, the wave generator successfully forms and transmits the desired wave structure. Because of the *bourrelet* focusing that takes place, we expect nonlinear effects to appear. Indeed, in the highlighted dashed region, the theoretical solution, which does not take nonlinear effects into account, differs significantly from the experimental wave field (see Fig. 14c), where small-scale structures can be observed in the focal region. The actual study of this instability is, however, beyond the scope of this article.

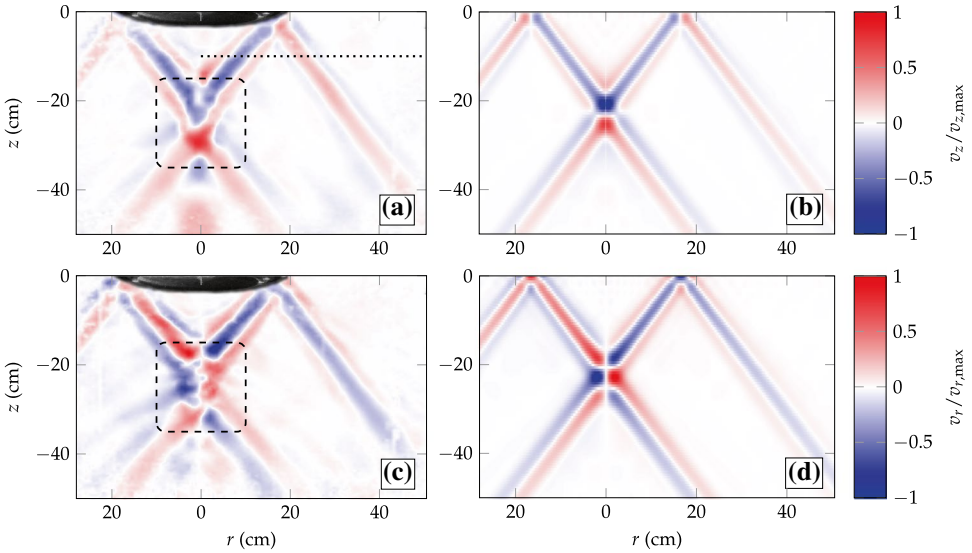

Fig. 14 Experimental measurements of the **a** vertical and **c** radial velocities in a vertical plane passing through the central axis of the generator. The generator is centered at $(z, r) = (0, 0)$ and set as a *bourrelet*, with $\omega/N = 0.85$ and $f/N = 0.2$. The dashed square highlights the area where nonlinear effects are apparent. Corresponding linear predictions obtained using Eq. (25) are shown in panels **b** and **d**

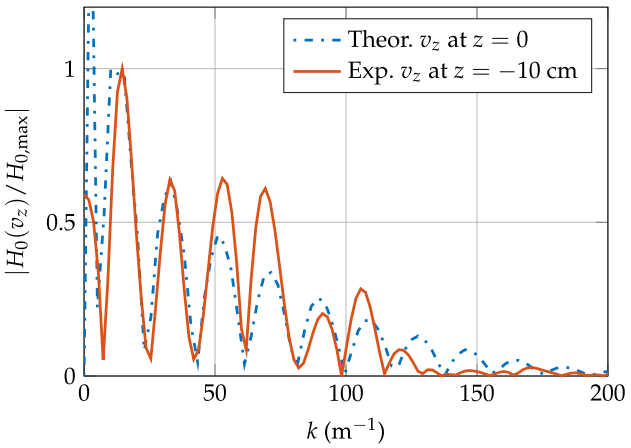

Fig. 15 Hankel transform (zeroth-order) of both the vertical velocity profile at $z = -10$ cm (the location of the radial profile is shown in Fig. 14b by a dotted line) and the corresponding theoretical profile (derived from the ring arrangement shown in Fig. 13a)

5 Conclusion

Starting with the internal wave generator of Gostiaux et al. (2006), we advance the design by converting the plates into rings in order to generate axisymmetric inertia-gravity waves. Unlike other axisymmetric wave generation studies (Duran-Matute et al. 2013; Le Dizès 2015), this system allows us to generate a controlled wave form by adjusting the amplitude and the offset of each cylinders. Starting with the decomposition of an axisymmetric internal wave field into its constituent Bessel modes, we model the linear propagation of the waves. We demonstrate the ability of the generator to produce two qualitatively different types of axisymmetric waves. The first is a truncated Bessel function for which PIV measurements in a horizontal and vertical plane were successfully collected. We demonstrate the quality of the wave generation in both a rotating and a non-rotating case. Moreover, we confirm the dispersion relation for various forcing and rotation frequencies, and we compare the emitted field with theory. The model and experimental wave fields are found to be in excellent agreement with the measured velocities. We also investigate the efficiency of the wave generator and find it to be operating reasonably close to maximum efficiency, with the exact degree of efficiency dependent on the external rotation rate.

The second configuration, which we name *le bourrelet*, highlights the possibility of generating unique axisymmetric wave structures. One key feature of the *bourrelet* is wave focusing. We show experimentally that, as wave focusing is established, the amplitude increase leads to wave instability.

Among the rich wave configurations and interactions offered by this new wave generator, some have caught our attention. To our knowledge, there is no mathematical description of internal wave instabilities in an axisymmetric context. Notably, the triadic resonant instability description would be challenging, as spatial resonance conditions are more complex when taking into account Bessel functions instead of plane waves. Our device is an interesting tool to emit a controlled Bessel mode and to study such kind of instability in an axisymmetric context, as was done previously with plane waves (Bourget et al. 2013; Ghaemsaidi et al. 2016; Maurer et al. 2016). Future work could reproduce an axisymmetric "storm-like" forcing at the surface, to mimic the action of a storm on the ocean, which could subsequently yield experimental insight into wave propagation and mixing in a highly relevant geophysical context. The role of rotation in the propagation and mixing processes can also be investigated in our setup, leading to geophysically relevant, complex experiments. Secondly, the *bourrelet* configuration shows

an interesting geometric focusing of a wave field that can be made more intriguing by altering the profile of the background stratification. For example, a non-uniform stratification can be used, where N changes with z, to tune the vertical transport of energy; the group velocity, which coincides with energy transmission, vanishes at z_0, where $N(z_0) = \omega$ (Paoletti and Swinney (2012). If the geometric focusing takes place at the same depth z_0, we expect a significant accumulation of energy and the formation of a localized, highly nonlinear phenomenon (Maurer 2017).

Acknowledgements We thank Neil Balmforth for insightful discussions. We thank M. Moulin and D. Le Tourneau for the design and production of the wave generator and the tank. This work has been achieved thanks to the resources of PSMN from ENS de Lyon. The team in Lyon also thanks CNRS and ENS de Lyon for providing the financial support to build the rotating platform PERPET. T. P. acknowledges the support of the NSF (OCE-1357434), as well as ENS de Lyon for providing funding for his visits in Lyon.

References

Alexander M, Holton J, Durran D (1995) The gravity-wave response above deep convection in a squall line simulation. J Atmos Sci 52(12):2212–2226. doi:10.1175/1520-0469(1995)052<2212:TGWRAD>2.0.CO;2

Alford M (2001) Internal swell generation: the spatial distribution of energy flux from the wind to mixed layer near-inertial motions. J Phys Ocean 31(8):2359–2368. doi:10.1175/1520-0485(2001)031<2359:ISGTSD>2.0.CO;2

Apel J, Byrne H, Proni J, Charnell R (1975) Observations of oceanic internal and surface-waves from earth resources technology satellite. J Geophys Res 80(6):865–881. doi:10.1029/JC080i006p00865

Bordes G, Venaille A, Joubaud S, Odier P, Dauxois T (2012) Experimental observation of a strong mean flow induced by internal gravity waves. Phys Fluids 24(8):086602. doi:10.1063/1.4745880

Bourget B, Dauxois T, Joubaud S, Odier P (2013) Experimental study of parametric subharmonic instability for internal plane waves. J Fluid Mech 723:1–20. doi:10.1017/jfm.2013.78

Cacchione D, Wunsch C (1974) Experimental study of internal waves over a slope. J Fluid Mech 66(02):223. doi:10.1017/S0022112074000164

Davis AMJ, Smith SGL (2010) Tangential oscillations of a circular disk in a viscous stratified fluid. J Fluid Mech 656:342–359. doi:10.1017/S0022112010001205

Delisi DP, Orlanski I (1975) On the role of density jumps in the reflexion and breaking of internal gravity waves. J Fluid Mech 69(3):445–464. doi:10.1017/S0022112075001516

Duran-Matute M, Flór JB, Godeferd FS, Jause-Labert C (2013) Turbulence and columnar vortex formation through inertial-wave focusing. Phys Rev E Stat Nonlinear Soft Matter Phys 87(4):1–4. doi:10.1103/PhysRevE.87.041001

Echeverri P, Flynn MR, Winters KB, Peacock T (2009) Low-mode internal tide generation by topography: an experimental and numerical investigation. J Fluid Mech 636(6):91. doi:10.1017/S0022112009007654

Ermanyuk EV, Shmakova ND, Flór JB (2017) Internal wave focusing by a horizontally oscillating torus. J Fluid Mech 813:695–715

Fincham A, Delerce G (2000) Advanced optimization of correlation imaging velocimetry algorithms. Exp Fluids 29(7):S013–S022. doi:10.1007/s003480070003

Flynn M, Onu K, Sutherland B (2003) Internal wave excitation by a vertically oscillating sphere. J Fluid Mech 494:65–93. doi:10.1017/S0022112003005937

Fortuin JMH (1960) Theory and application of two supplementary methods of constructing density gradient columns. J Polym Sci 44(144):505–515. doi:10.1002/pol.1960.1204414421

Ghaemsaidi SJ, Joubaud S, Dauxois T, Odier P, Peacock T (2016) Nonlinear internal wave penetration via parametric subharmonic instability. Phys Fluids 28(1):011703. doi:10.1063/1.4939001

Ghaemsaidi SJ, Peacock T (2013) 3D Stereoscopic PIV visualization of the axisymmetric conical internal wave field generated by an oscillating sphere. Exp Fluids 54(2):1454. doi:10.1007/s00348-012-1454-6

Görtler H (1943) Uber eine Schwingungserscheinung in Flussigkeiten mit stabiler Dichteschichtung. ZAMM J Appl Math Mech Z Angew Math Mech 23(2):65–71. doi:10.1002/zamm.19430230202

Gostiaux L, Didelle H, Mercier S, Dauxois T (2006) A novel internal waves generator. Exp Fluids 42(1):123–130. doi:10.1007/s00348-006-0225-7

Halpern D (1971) Observations on short-period internal waves in Massachusetts bay. J Mar Res 29(2):116

Haury L, Briscoe M, Orr M (1979) Tidally generated internal wave packets in Massachusetts Bay. Nature 278(5702):312–317. doi:10.1038/278312a0

Ivey G, Winters K, Koseff J (2008) Density stratification, turbulence, but How much mixing? Annu Rev Fluid Mech 40(1):169–184. doi:10.1146/annurev.fluid.39.050905.110314

King B, Zhang HP, Swinney HL (2010) Tidal flow over three-dimensional topography generates out-of-forcing-plane harmonics. Geophys Res Lett. doi:10.1029/2010GL043221

Künze E, MacKay C, McPhee-Shaw EE, Morrice K, Girton JB, Terker SR (2012) Turbulent mixing and exchange with interior waters on sloping boundaries. J Phys Ocean 42(6):910–927. doi:10.1175/JPO-D-11-075.1

Le Dizès S (2015) Wave field and zonal flow of a librating disk. J Fluid Mech 782(2015):178–208. doi:10.1017/jfm.2015.530

Lee C, Beardsley R (1974) Generation of long nonlinear internal waves in a weakly stratified shear-flow. J Geophys Res Oceans 79(3):453–462. doi:10.1029/JC079i003p00453

Lighthill J (1978) Waves in fluids, 3rd edn. Cambridge University Press, Cambridge

Maas LRM, Benielli D, Sommeria J, Lam FPA (1997) Observation of an internal wave attractor in a confined, stably stratified fluid. Nature 388(6642):557–561. doi:10.1038/41509

Mathur M, Peacock T (2009) Internal wave beam propagation in non-uniform stratifications. J Fluid Mech 639:133. doi:10.1017/S0022112009991236

Maurer P (2017) Approche expérimentale de la dynamique non-linéaire d'ondes internes en rotation. Ph.D. thesis, École Normale Supérieure de Lyon

Maurer P, Joubaud S, Odier P (2016) Generation and stability of inertia-gravity waves. J Fluid Mech 808(1):539–561. doi:10.1017/jfm.2016.635

Maxworthy T (1979) Note on the internal solitary waves produced by tidal flow over a 3-dimensional ridge. J Geophys Res Oceans Atmos 84(NC1):338–346. doi:10.1029/JC084iC01p00338

Mercier MJ, Martinand D, Mathur M, Gostiaux L, Peacock T, Dauxois T (2010) New wave generation. J Fluid Mech 657:308–334

Messio L, Morize C, Rabaud M, Moisy F (2008) Experimental observation using particle image velocimetry of inertial waves in a rotating fluid. Exp Fluids 44:519–528

Moore CD, Koseff JR, Hult EL (2016) Characteristics of bolus formation and propagation from breaking internal waves on shelf slopes. J Fluid Mech 791(02):260–283. doi:10.1017/jfm.2016.58

Mowbray DE, Rarity BSH (1967) The internal wave pattern produced by a sphere moving vertically in a density stratified liquid. J Fluid Mech 30(03):489. doi:10.1017/S0022112067001569

Oster G, Yamamoto M (1963) Density gradient techniques. Chem Rev 63(3):257–268. doi:10.1021/cr60223a003

Paoletti MS, Swinney HL (2012) Propagating and evanescent internal waves in a deep ocean model. J Fluid Mech 706(7):571–583. doi:10.1017/jfm.2012.284

Peacock T, Mercier MJ, Didelle H, Viboud S, Dauxois T (2009) A laboratory study of low-mode internal tide scattering by finite-amplitude topography. Phys Fluids 21(12):1–4. doi:10.1063/1.3267096

Peacock T, Weidman P (2005) The effect of rotation on conical wave beams in a stratified fluid. Exp Fluids 39(1):32–37. doi:10.1007/s00348-005-0955-y

Smith S, Crockett J (2014) Experiments on nonlinear harmonic wave generation from colliding internal wave beams. Exp Thermal Fluid Sci 54:93–101. doi:10.1016/j.expthermflusci.2014.01.012

Teoh S, Ivey G, Imberger J (1997) Laboratory study of the interaction between two internal wave rays. J Fluid Mech 336(01):91–122. doi:10.1017/S0022112096004508

Thomas JA, Lerczak JA, Moum JN (2016) Horizontal variability of high-frequency nonlinear internal waves in Massachusetts Bay detected by an array of seafloor pressure sensors. J Geophys Res Oceans 121(8):5587–5607. doi:10.1002/2016JC011866